Genetic Interaction of APOE-$\varepsilon 4$ and PICALM rs3851179 is Associated With Dynamic Functional Connectivity in Healthy Middle-Aged Adults at Risk for Alzheimer's Disease

Shyamal Y. Dharia [1], Camilo E. Valderrama [1,3], Qian Liu [1,4], and Stephen D. Smith [1,2,✉]

[1]Department of Applied Computer Science, The University of Winnipeg, Winnipeg, Canada; [2]Department of Psychology, The University of Winnipeg, Winnipeg, Canada; [3]Department of Community Health Sciences, Cumming School of Medicine, University of Calgary, Calgary, Canada; [4]Department of Biochemistry and Medical Genetics, Max Rady College of Medicine, University of Manitoba, Winnipeg, Canada

Background: Alzheimer's disease (AD) is a neurodegenerative disorder in which genetic risk variants, including APOE ε4 (A+) and the PICALM rs3851179 variant (P+), are linked to altered brain function.

Objective: To test whether dynamic functional connectivity (dFC) dwell-time patterns from resting-state fMRI differ by AD genetic risk in cognitively healthy, middle-aged adults.

Methods: We estimated recurring dFC clusters from rs-fMRI and computed dwell time (total time spent in each cluster) for individuals in not-at-risk, A+P−, and A+P+ groups. Group differences in dwell-time profiles were assessed, and logistic regression with permutation testing evaluated the association between dwell-time features and genotype.

Results: At-risk groups (A+P−, A+P+) spent less time in left-hemisphere hubs than not-at-risk individuals, consistent with reports of left-hemisphere vulnerability in AD. Logistic regression showed modest above-chance genotype discrimination, with permutation tests indicating a marginal trend when comparing not-at-risk versus at-risk (A+P−, A+P+) groups.

Conclusions: Dwell-time features from dFC states show preliminary sensitivity to AD genetic risk and warrant evaluation in larger samples as potential early risk markers. Our code is available on GitHub.

Alzheimer's Disease | Dynamic Functional Connectivity | Dwell-time | Clustering

Correspondence: ***s.smith@uwinnipeg.ca***

Introduction

Alzheimer's disease (AD) is a neurodegenerative disorder involving progressive memory loss and the deterioration of executive functions (Scharre, 2019; Rao et al., 2022). Although symptoms of AD are typically reported after the age of 65, psychometric tests can sometimes detect subtle declines in cognitive abilities and social engagement up to a decade earlier (Langbaum et al., 2020). Such results suggest that there are potential behavior patterns and biomarkers that can predict the likelihood that an individual will develop AD (see Breijyeh and Karaman (2020), for a review). The challenge for researchers is to identify these markers in order to provide patients and clinicians with the earliest possible indicator of potential AD so that physicians can prescribe medications that could slow the progression of the disease.

A key factor in the early identification of AD relates to its underlying neuropathology. Cellular studies of AD have consistently identified two hallmark features—extracellular deposits of beta-amyloid ($A\beta$) and intracellular neurofibrillary tangles composed of twisted tau filaments (Brion, 1998). The neural locations of these pathologies are not random. $A\beta$ initially accumulates in medial prefrontal and medial parietal regions before progressing to temporal-lobe structures (Palmqvist et al., 2017). The tau filaments are first detected in temporal-lobe structures related to memory, including the entorhinal cortex, parahippocampal cortex, and hippocampus (Small et al., 2011). Importantly, these changes in the brain's structure are often present before the appearance of clinical symptoms (Jack et al., 2013, 2019), thus highlighting the need for methods of early identification of at-risk individuals.

One intuitive method of early detection of Alzheimer's susceptibility is genetic testing. Genetic researchers have identified numerous genes that increase an individual's risk for developing AD (Breijyeh and Karaman, 2020). Specifically, Apolipoprotein (APOE)-$\varepsilon 4$ has been found to be the strongest genetic risk factor for AD and is associated with increased levels of $A\beta$ deposits and an earlier age of onset (M Di Battista et al., 2016). Structural neuroimaging studies found that these Aβ deposits affected the hippocampus; APOE-$\varepsilon 4$ carriers exhibited smaller left hippocampal volumes than non-carriers of this gene (Wang et al., 2015). Additionally, a large body of work indicates that the phosphatidylinositol-binding clathrin assembly protein (PICALM) gene influences AD risk primarily by modulating the production, transport, and clearance of $A\beta$ (Xu et al., 2015). Therefore, studying both APOE-$\varepsilon 4$ and PICALM in genetically at-risk but otherwise healthy

individuals could provide promising and novel avenues for understanding early AD diagnosis and for therapeutic development. For instance, a recent study (Morgen et al., 2014) found that the interaction between APOE-$\varepsilon 4$ and PICALM rs3851179 adversely affects the cognitive performance (Trail Making Test A) and brain atrophy (prefrontal), respectively, in patients with early AD dementia. Thus, it is equally important to examine the functional impact of APOE-$\varepsilon 4$ and PICALM rs3851179 on the brain to gain a more comprehensive understanding of their roles in early AD.

One neuroimaging tool that has been used to assess neural changes in AD is resting-state functional magnetic resonance imaging (rs-fMRI). This brain-imaging technique measures low-frequency fluctuations in the blood-oxygen-level-dependent (BOLD) signal while participants lie quietly without engaging in any task. Analysis of these BOLD fluctuations consistently shows a set of spatially distributed but temporally coherent resting-state networks (Raichle et al., 2001). Numerous resting-state networks have been identified. Prominent among these are the (1) Visual, (2) Sensorimotor, (3) Dorsal Attention, (4) Ventral Attention, (5) Salience (SN) Ventral Attention, (6) Limbic, (7) Frontoparietal, and (8) Default-mode (DMN; see Raichle, 2015 (Raichle, 2015), for a review). In AD and mild cognitive impairment (MCI), disrupted connectivity has been most consistently observed in the DMN, arguably because its core hubs (i.e., posterior cingulate, hippocampus) are early sites of amyloid and tau pathology (Mintun et al., 2006). Studies finding alterations of rs-fMRI in the DMN (Allen et al., 2007; Greicius et al., 2004; Li et al., 2002) primarily have found decreased connectivity. A smaller body of work suggests that DMN decrease connectivity may be accompanied by compensatory increase in connectivity in frontal executive regions (Agosta et al., 2012) or the SN (Zhou et al., 2010).

Importantly, the genetic variants that increase AD risk also modulate intrinsic brain networks before any clinical evidence of pathology. For example, one study observed that participants carrying an APOE-$\epsilon 4$ allele had clear indications of abnormalities in precuneus resting-state functional connectivity in the absence of any cognitive impairment, and in the absence of fibrillar cerebral ($A\beta$) deposits detectable by positron emission tomography imaging (Sheline et al., 2010). A recent study (Dzianok et al., 2025b) found that individuals carrying the APOE-$\epsilon 4$ allele exhibited reduced network strength in the posterior (temporo-occipital) portion of the middle temporal gyrus, compared with non-carriers, when independent components of the DMN were analyzed. Likewise, in a cohort of 283 young adults, PICALM G-allele carriers showed weaker connectivity compared with AA carriers in the hippocampal region (Zhang et al., 2015). However, although these studies provide important information about functional connectivity in individuals genetically at risk for AD, they estimate network connectivity by averaging patterns over the entire resting-state fMRI scan (e.g., approximately 7-10 minutes). Recent advances in analysis techniques now enable researchers to track changes in functional connectivity throughout a resting-state scan (Hutchison et al., 2013; Preti et al., 2017). By capturing these brief connectivity states, they can directly link time-varying network changes to cognitive processes and behavior (Hutchison et al., 2013).

Dynamic resting-state functional connectivity (dFC) divides the BOLD time series into overlapping sliding windows (e.g., 30–60 s) and computes a separate connectivity matrix for each window (Hutchison et al., 2013; Preti et al., 2017). These windowed matrices are then clustered into a finite set of recurring connectivity states, each reflecting a distinct pattern of inter-regional coupling (Allen et al., 2012). From these states, we derive features such as dwell-time, the average number of windows an individual remains in a given state, and fractional occupancy, the proportion of total scan time spent in each state. For example, Jones et al.(Jones et al., 2012) found a significant difference in dwell-time between AD and cognitively healthy groups. Another study found that differences in dFC strength in the left precuneus, default mode network, and dorsal attention network among normal controls, aMCI patients, and AD patients (Zhao et al., 2022). Finally, linking dFC with genetic literature related to AD, Gong et al. (Gong et al., 2025) reported that APOE-$\epsilon 4$ modulates fluctuating communication within the cerebellar lobe and the dFC between the cerebellar lobe and the temporal gyrus in AD. To date, no rs-fMRI study has examined dFC changes associated with the PICALM gene; however, an electroencephalogram (EEG) study (Ponomareva et al., 2020) found lower functional connectivity in PICALM GG carriers, suggesting early functional changes in the alpha frequency band.

In this study, we build upon this earlier dFC research to examine whether the dwell time of resting-state networks varies across genotypes. Specifically, we use rs-fMRI data from the Polish Electroencephalography (EEG), Alzheimer's Risk-genes, Lifestyle and Neuroimaging (PEARL-Neuro) Database (Dzianok and Kublik, 2024) to compare healthy middle-aged individuals who had both the APOE-$\epsilon 4$ allele and the PICALM gene (i.e., the double-risk group), individuals with the APOE $\epsilon 4$ allele but not the PICALM gene, or individuals who did not have either AD-related allele. We specifically hypothesized that differences in dwell time would be observed between the double-risk group and the no-risk group. These results would provide a novel biomarker for AD susceptibility and may provide insight into the neural mechanisms underlying the early symptoms of this disorder.

Methods

A. Participants

In this study, PEARL-Neuro Database (Dzianok and Kublik, 2024), freely available online at the OpenNeuro database, is utilized. Our study specifically focuses on rs-fMRI data, which consists of 68 healthy middle-aged subjects. In the previous study (Dzianok et al., 2025a), these subjects were divided into three different categories based on their genetic risk factors for AD: (1) no-risk gene (APOE ε4/PICALM rs3851179 variants are absent, A-P- or N), (2) single-risk gene (APOE ε4 present/PICALM rs3851179 absent, A+P-), (3) double-risk gene (APOE ε4/PICALM rs3851179 variants are both present, A+P+) to find AD-like features in rs-EEG/fMRI data. The distribution of subjects in each group is shown in Table 1. For all subjects, the Edinburgh Handedness Inventory (EHI) test result confirmed right-handedness, and all subjects were generally healthy with no decline in cognitive task performance. This research received ethics approval from the University of Winnipeg Human Research Ethics Board.

B. Scanning Parameters

The rs-fMRI and structural MRI (T1w and T2w) data from the PEARL database were recorded on a Siemens Prisma FIT 3 T scanner (Siemens Medical Systems, Erlangen, Germany) using a gradient-echo EPI sequence with repetition time (TR) = 0.8 s, echo time (TE) = 38 ms, slice thickness = 2 mm, and voxel size = $2 \times 2 \times 2\,\text{mm}^3$. Images were taken with two-phase encoding directions: Anterior-to-Posterior (AP) and Posterior-to-Anterior (PA) for approximately 7.5 minutes each.

C. fMRI Preprocessing

First, since the fMRI data were recorded using two-phase encoding directions (AP and PA), we corrected the geometric distortions that occur in fMRI scans by applying FSL topup correction (Andersson et al., 2003). These distortions are usually caused by static magnetic field inhomogeneities, leading to pixel shifts, particularly in the phase encode direction (Jezzard and Balaban, 1995). The FSL top-up correction was conducted by taking a mean of the whole AP and PA scans (volume dimensions $108 \times 108 \times 72$ voxels), and then estimating distortions in the AP and PA rs-fMRI scans for each subject. After the distortions were found, we applied a top-up method to correct these distortions from both scans for each subject.

Subsequently, we used a well-established pipeline, fMRIprep (Esteban et al., 2019, 2020), to further enhance our data preprocessing. The undistorted data from AP and PA scans underwent the following steps using fMRIprep: a reference volume was generated and used to estimate and correct head motion (via FSL mcflirt); each scan was then co-registered to the subject's T1w image using FreeSurfer's boundary-based registration and FSL flirt (6 degrees of freedom), and all spatial transforms (motion, distortion correction, anatomical alignment and normalization to Montreal Neurological Institute (MNI) space) were composed into a single interpolation step. The coregistration template that we used was the MNI 152 Nonlinear 2009cAsym template (Fonov et al., 2011, 2009). The final volume dimensions after fMRIprep, both AP and PA scans, were $97 \times 115 \times 97 \times 560$ voxels, where the first three dimensions were spatial (voxels) and the fourth dimension ($t = 560$) was the number of time points sampled with TR = 0.8s. Alongside the preprocessed images, fMRIPrep generates a set of confound regressors for each functional run, which were not removed in prior steps. From those regressors, six head motion parameters, translations (x, y, z) and three rotations (pitch, roll, yaw), were selected and subsequently regressed out from the BOLD time-series data to mitigate the effects of subject motion.

D. Correlation Computation and Clustering

After the AP and PA scans were cleaned, we extracted correlation matrices across seven brain networks: (1) Visual, (2) Somatomotor, (3) Dorsal Attention, (4) Salience/Ventral Attention, (5) Limbic, (6) Control, and (7) DMN. These networks are used in many fMRI studies, and they involve a wide range of brain structures, some of which are closely associated with AD. For instance, the hippocampus, part of several networks and a sub-region of the DMN, often shows weaker functional connectivity and structural loss in AD (Andrews-Hanna et al., 2010; Zhou et al., 2008; O'Callaghan et al., 2019; Lee et al., 2020). Similar AD-related changes have been found in the other six networks, motivating our decision to focus on this set of seven large-scale networks for subsequent analyses.

We used the 100-parcel, 7-network Schaefer atlas, which is aligned to the MNI 152 Nonlinear 2009cAsym template employed in preprocessing, and splits every network into its specific subregions (e.g., medial prefrontal cortex, precuneus). This provides 100 non-overlapping parcels that cover the whole cortex. Furthermore, using these 100 parcels, we computed sliding–window correlations. The sliding window moves across the entire duration of the scans with a fixed 16s window (16s/0.8s per TR = 20 volumes) with 75% overlap. A 75% overlap was chosen to ensure that brief or boundary-adjacent fluctuations in functional connectivity were captured and to reduce variance in our correlation estimates. Consequently, for each subject, the resulting correlation matrices across both scans had dimensions $100 \times 100 \times 218$, where 218 was the total number of windows across both scans (109 per scan). This was computed as $(560 - 20)/5 = 109$, where 560 is the number of volumes per scan, 20 is the window size in volumes, and 5 is the step size (i.e., 25% of 20). For each window $w = 1, \ldots, W$, the correlations across all parcellated regions were computed by first calculating

Table 1. Description of the study participants by group

Group	Final Count	Ratio (%)	Age (Mean ± SD)	Sex Distribution
N	27	39.7	55.2 ± 2.9	F: 15, M: 12
A+P-	23	33.8	55.7 ± 3.3	F: 12 , M: 11
A+P+	18	26.5	55.7 ± 3.4	F: 8 , M: 10
Total	**68**	**100.0**	$\mathbf{55.5 \pm 3.1}$	**F: 35 , M: 33**

the pairwise covariance and variances in window w:

$$\varepsilon_{ij}^{(w)} = \mathrm{Cov}\big(X_i^{(w)}, X_j^{(w)}\big), \quad i,j = 1,\ldots,n, \tag{1}$$

$$\Sigma_{ii}^{(w)} = \mathrm{Var}\big(X_i^{(w)}\big), \quad \Sigma_{jj}^{(w)} = \mathrm{Var}\big(X_j^{(w)}\big). \tag{2}$$

Then the Pearson correlation for each pair (i,j) is

$$R_{ij}^{(w)} = \frac{\varepsilon_{ij}^{(w)}}{\sqrt{\Sigma_{ii}^{(w)}\,\Sigma_{jj}^{(w)}}}, \quad i,j = 1,\ldots,n, \tag{3}$$

where $X_i^{(w)}$ is the time series of parcel i in window w, $\mu_i^{(w)} = \mathbb{E}[X_i^{(w)}]$ its mean, and $\varepsilon_{ij}^{(w)}$ the covariance between parcels i and j in that window.

Finally, since correlation FC does not contain any directional information and produces a symmetric (mirror) square matrix, we only used the lower-triangular entries and used these feature vectors as input to K–means clustering with K clusters. Rather than selecting a single fixed value of K, we explored a range of cluster numbers. The lower bound of this range was informed by the elbow method (Figure 1), which identifies a point of diminishing returns in within-cluster variance reduction. The upper bound was determined empirically by examining the distribution of subjects across clusters: beyond a certain value of K, some clusters contained very few windows from only a handful of subjects, reducing statistical power and interpretability. The shaded region in Figure 1 reflects this valid K-range, bounded by values where cluster formation remained both stable and statistically meaningful for group-level analysis. To visualize the clusters, we applied principal component analysis (PCA) to reduce the 4950 (100*99/2) connectivity pairs to two dimensions and plotted each sample by its cluster assignment to visualize cluster formation.

E. Feature Extraction and Statistical Methods

After utilizing K-means clustering, we computed the *dwell-time* of each subject within each cluster. This was defined as the total time spent in a given cluster, calculated by:

$$\mathrm{DT}_k = N_k \times W_{\mathrm{step}} \times \mathrm{TR}, \tag{4}$$

where N_k is the number of FC windows assigned to cluster k, W_{step} is the sliding-window step size measured in volumes (here $W_{\mathrm{step}} = 5$ volumes, corresponding to $5 \times \mathrm{TR} = 4\mathrm{s}$), and TR is the repetition time ($0.8\mathrm{s}$). The sliding window length was 20 volumes (16s), producing a 75% overlap when using a 5-volume step (4s).

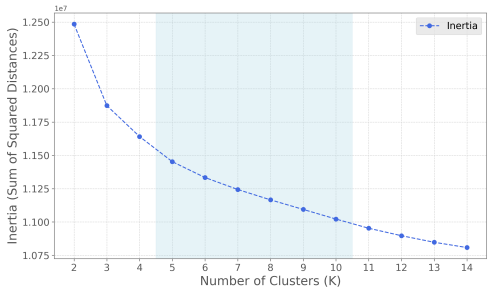

Figure 1. Elbow method for selecting the optimal number of clusters k in K-means clustering. The x-axis shows the number of clusters (k), and the y-axis shows the within-cluster sum of squares (inertia). The highlighted k values were used for both statistical analysis and machine learning.

For each value of K, we tested whether dwell time for each cluster differed across genetic risk groups (N, A+P- and A+P+) using an adaptive statistical approach. For each cluster, we first assessed the assumptions required for parametric testing by applying the Shapiro-Wilk test for normality within each group and Levene's test for homogeneity of variance across groups. When both normality ($p > 0.05$) and variance homogeneity ($p > 0.05$) assumptions were satisfied, we used parametric tests: t-test for two-group comparisons (for machine learning) or ANOVA for multi-group comparisons (for initial statistical analysis). When these assumptions were violated, we employed non-parametric alternatives: the Mann-Whitney U test for two groups or the Kruskal-Wallis test for multiple groups. To control the family–wise error across the K clusters, the resulting (p)-values were corrected using the Benjamini—Hochberg false discovery rate (FDR) procedure; clusters with FDR-corrected ($p < 0.05$) were deemed significant.

F. Hubness Analysis via Statistical Testing

After the K-means clustering, we selected clusters producing significant or lowest p-values between-group differences ($p < 0.05$) in dwell-time and extracted their 1D correlation vectors, then reconstructed them into symmetric 100×100 connectivity matrices for each sample within those clusters. We then computed the global mean connectivity matrix by averaging all connectivity matrices (alternatively, by using the cluster centroid) across all subjects and groups within each significant cluster, under the assumption that clustered windows reflect a common network configuration that transcends group boundaries while still showing differential dwell-time patterns. This global approach allows us to mea-

sure the underlying connectivity that defines each significant cluster, providing insight into the network topology that groups differentially occupied in time. As the dwell-time feature represents how much time a subject spent in a given cluster, we chose to use hubness analysis on this global connectivity pattern to identify dominant "sink" regions that measure each network configuration. This approach helps link temporal dynamics (i.e., dwell-time differences between groups) with spatial topological features (i.e., globally consistent hub regions), providing a unified interpretation of how genotype-specific temporal patterns emerge within shared connectivity configurations.

To identify the top 10 hub regions within each significant cluster, we established a threshold by computing the median plus two standard deviations of this global mean connectivity matrix, which corresponds to approximately the top 2—3% of connectivity values. We then binarized the global connectivity matrix using this threshold and computed hubness proportions for each region by summing its corresponding row in the binary matrix and dividing by the total number of regions minus one (99). The ten regions with the highest hubness proportions from each significant (lowest p-value) cluster were aggregated across all K values and multiple random seeds to identify the most consistently appearing hub regions.

G. Machine learning

As a complementary analysis, we applied a simple machine learning classifier to test whether dwell-time features could generalize to unseen data. Specifically, we used logistic regression to predict genotype groups based on dFC dwell-time profiles. This analysis helped evaluate the potential of these functional markers in distinguishing at-risk individuals, beyond group-level statistics. Figure 2 illustrates the comprehensive workflow for genotype prediction using dwell-time features. We framed the genotype prediction task as a set of binary classifications comparing groups N, A+P-, and A+P+ as N vs A+P-, N vs A+P+, A+P- vs A+P+, and N vs (A+P- and A+P+ combined). The overall pipeline consists of several sequential steps:

G.1. Data Preprocessing and Cross-Validation Setup. First, we ensured that the functional connectivity matrices (100×100) were flattened into 1D vectors containing 4,950 unique connectivity features, which served as the required input format for k-means clustering. Subjects were then partitioned into training and testing folds using stratified 10-fold cross-validation.

G.2. Training Phase. Within each training fold, k-means clustering was performed exclusively on training data to identify K connectivity clusters (where K ranges from 5 to 10). Based on these cluster assignments, we compute each subject's dwell-time, the total time spent in each connectivity cluster. To select the most discriminative cluster, we employ adaptive statistical testing that first evaluates normality (Shapiro-Wilk test) and variance homogeneity (Levene's test) assumptions. Depending on whether these assumptions were satisfied, we apply either parametric tests (t-test) or non-parametric alternatives (Mann-Whitney U test). The cluster with the lowest p-value was selected, and the dwell-time feature was extracted. Finally, the single dwell-time feature was used to train a logistic regression model. Therefore, in one run, six logistic regression models trained considering the K = 5 to 10 range were used.

G.3. Test Phase. Crucially, the same k-means model trained on the training data was applied to assign test subjects to clusters, ensuring no data leakage occurs since test data never influences cluster construction. Dwell-time features were extracted from test subjects using the previously identified optimal cluster, and predictions were generated using the corresponding trained logistic regression model.

G.4. Ensemble Method. This process was repeated across K = 5 to 10 clusters and five random seeds for stability, resulting in six logistic regression models per seed. To combine predictions across different K values for one seed run, we implement a p-value weighted ensemble method where models with lower p-values received higher weights in the final prediction. The weights were computed as follows:

$$w_k = \frac{(1/p_k + \epsilon)^\alpha}{\sum_{j=5}^{10}(1/p_j + \epsilon)^\alpha} \quad \textbf{(5)}$$

Where p_k was the p-value for cluster K, p_j was the p-value for cluster j in the denominator sum, where j ranges from 5 to 10, $\varepsilon = 10^{-10}$ was a smoothing parameter to prevent division by zero, and $\alpha = 2$ was the power parameter that emphasizes models with lower p-values. Finally, the prediction was computed as follows:

$$P_{\text{ensemble}}(\hat{y} = 1 \mid x) = \sum_{k=5}^{10} w_k \, P_k(y = 1 \mid x), \quad \textbf{(6)}$$

$$\hat{y} = \begin{cases} 1, & \text{if } P_{\text{ensemble}}(y = 1 \mid x) > 0.5, \\ 0, & \text{otherwise.} \end{cases} \quad \textbf{(7)}$$

where $P_k(\hat{y} = 1 \mid x)$ was the predicted probability from the logistic regression model trained using K clusters, and $\hat{y}_{\text{ensemble}}$ was the final binary prediction. This weighted-ensemble approach prioritizes models that demonstrate stronger statistical evidence for group differences.

H. Performance Evaluation and Model Interpretability

Performance was evaluated using accuracy, precision, recall, F1-macro and Area under the Receiver Operating Characteristic Curve (AUC-ROC). For each seed,

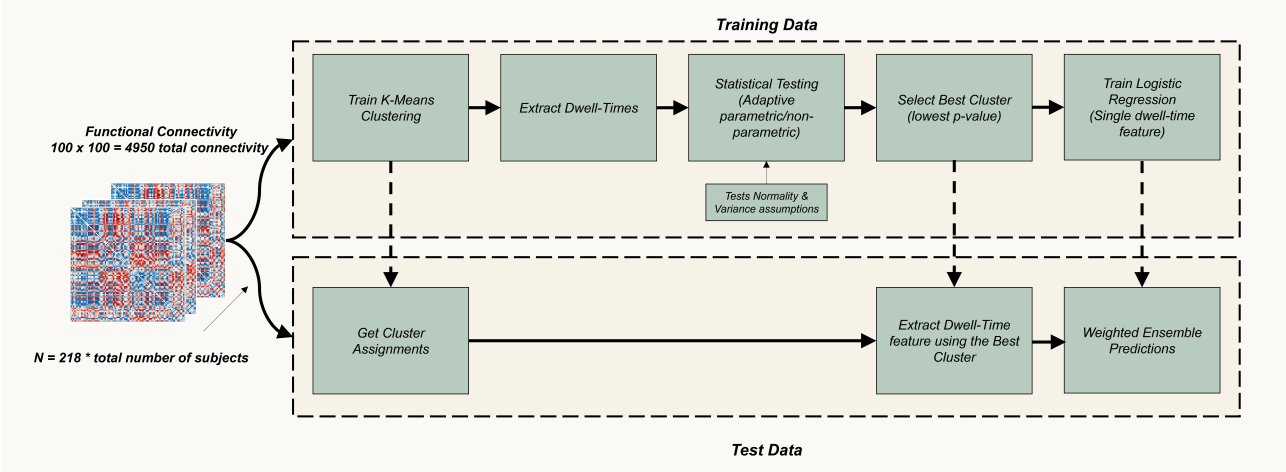

Figure 2. fMRI dynamic connectivity classification pipeline. Flowchart illustrating the machine learning approach for classifying genetic risk groups based on dwell-time feature. The pipeline uses K-means clustering, statistical testing to select the best discriminative cluster based on dwell-time features, and weighted ensemble methods to combine predictions across different numbers of clusters (K=5-10). Strict train-test separation prevents data leakage throughout the cross-validation procedure.

we averaged each metric across the 10 folds; the final reported score for each metric is the mean $\pm$ standard deviation across the five seeds. All preprocessing (including feature standardization) and feature selection were performed using *training data* only. For reproducibility, K-means initialization and fold generation were seeded (with different seeds) for each run.

To show the interpretation of our logistic regression models, we extracted coefficients from each fold and back-transformed them from scaled values to their original units of seconds. This transformation enabled the interpretation of how dwell-time in statistically significant connectivity clusters correlates with genetic risk group membership. We computed effect sizes at the 16-second time scale, corresponding to our sliding window length. The resulting coefficient indicated the change in log-odds per additional 16 seconds of dwell-time.

H.1. Permutation Test. To assess the statistical significance of our classification results and ensure they were not due to chance, we performed a permutation test for each classification task. This procedure tests the null hypothesis that there is no true association between dwell-time features and genotype labels. To test this, for each task, the entire classification pipeline was first run with the correct subject-label assignments to calculate the observed AUC. Then, the procedure was repeated 1,000 times. In each repetition, the genotype labels were randomly shuffled across subjects, thereby breaking any true relationship between the features and the labels, while preserving the data shape of dwell-time features and the imbalance between groups. This process generated a null distribution of AUC scores, representing the range of performance expected purely by chance. The empirical p-values are calculated as follows:

$$p_{AUC} = \frac{\sum_{i=1}^{N} \mathbf{1}(\text{AUC}_{\text{perm},i} \geq \text{AUC}_{\text{obs}}) + 1}{N+1} \quad \textbf{(8)}$$

This is an empirical permutation testing approach where the p-value represents the probability of observing a test statistic (AUC) as high or higher than the observed value under the null hypothesis of no group differences.

Results

I. Statistical Analysis

Our statistical analysis was focused on dwell-time features derived from k-means clustering using dFC windows, which were evaluated across a range of k values (k=5 to 10). This analysis consistently revealed two distinct clusters that demonstrated opposing patterns of dwell-time between subject groups (see Figure 3). For instance, at k=7, we observed that cluster 5 was characterized by significantly longer dwell-times for the N group compared to the A+P- and A+P+ group, whereas cluster 0 was characterized by marginally significant shorter dwell-times for the N group compared to the A+P- group. This pattern of two opposing clusters, one with increased dwell-time for the N group and another with decreased dwell-time, was a consistent trend across most k-values and random seeds. The large distance between the centroids of these two clusters suggests they represent fundamentally different functional connectivity patterns rather than minor variations of a single cluster. It is important to note that while these group differences were prominent, they did not survive the primary statistical correction for multiple comparisons across all clusters, and only some survived post-hoc p-value correction.

J. Hubness Analysis

To identify cluster configurations that distinguished the groups, we analyzed the most consistent regions of interest (ROIs) that act as hubs within those clusters. Tables 2 and 3 present the top 10 ROIs for the clusters in which the N group showed higher and lower dwell-

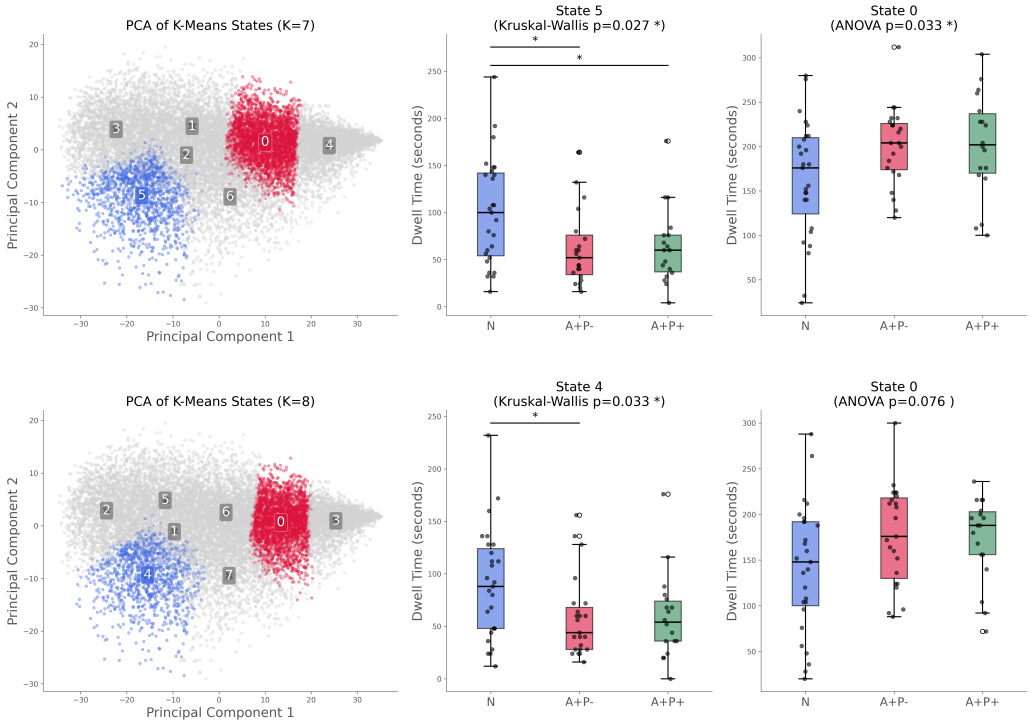

Figure 3. Discriminative clusters for K-means clustering with K=7 and K=8. Left panels show clustered PCA projections of functional connectivity windows, where the top two significant clusters are colored by group differences: blue indicates higher dwell time for the N group, red indicates higher dwell time for A+P-/A+P+ groups, and gray represents non-significant clusters. Right panels display corresponding box plots comparing dwell times between groups, with asterisks indicating significance levels.

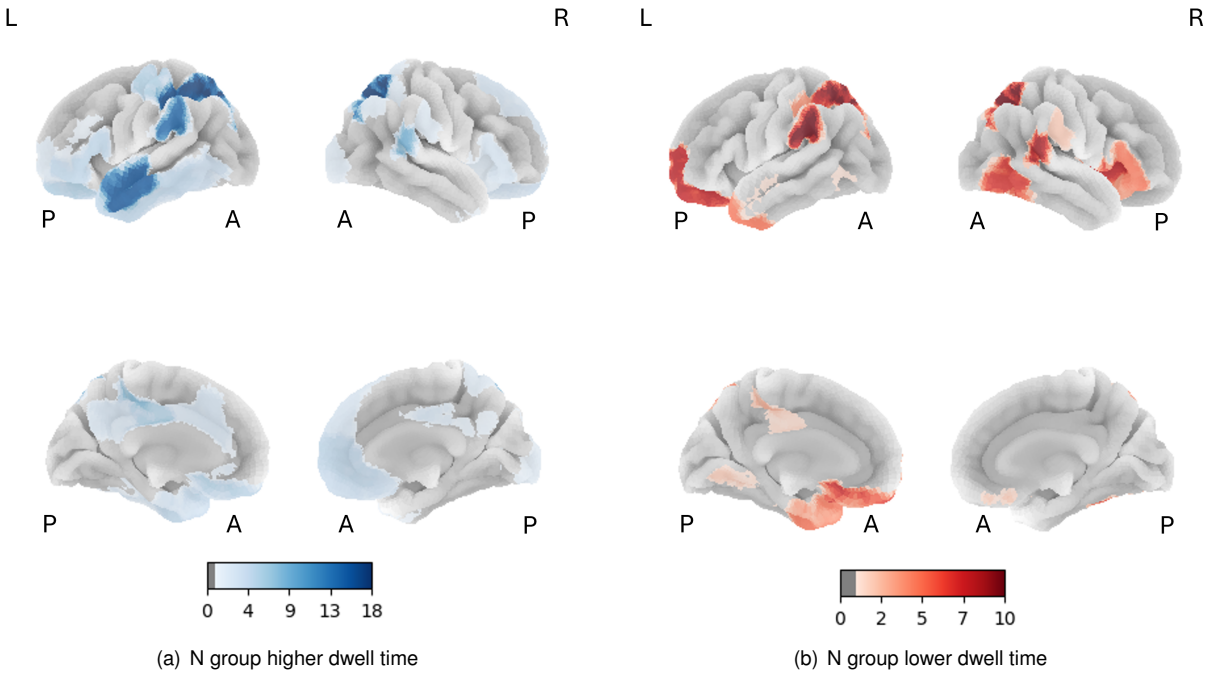

(a) N group higher dwell time

(b) N group lower dwell time

Figure 4. Comparative hub frequency maps for dFC clusters. Left panel (a): hub regions for clusters where not-at-risk (N) show higher dwell time; Right panel (b): hub regions for clusters where not-at-risk (N) show lower dwell time. Color intensity indicates frequency across significant clusters ($p < 0.05$, K = 5-–10). "L" and "R" indicate left and right hemispheres, and "A" and "P" indicate anterior and posterior. The top row represents lateral views, and the bottom row represents medial views.

times, respectively (aggregated across all k values and five random seeds). A pronounced left-hemisphere lateralization was evident in the clusters where the N group exhibited higher dwell-time relative to A+P-; specifically, eight of the ten top ROIs in those clusters were left-hemisphere regions. In the cluster showing the opposite trend, hemispheric hubs were approximately equally distributed between the two hemispheres. The total frequency of hub appearances was greater in the cluster associated with increased dwell-time for the N group, suggesting that this dFC pattern may represent a more stable or recurrent neural configuration. Figures 4(a)

Table 2. Top 10 Most Frequent Hub Regions (N Group Higher Dwell Time clusters). ROI indices and region names correspond to the Schaefer (2018) 100-parcel atlas. The *Freq* column shows frequency across seeds, and the *Avg Conn* column indicates average connectivity strength for that region.

Rank	ROI	Freq	Avg Conn	Hemi	Network	Atlas Region
1	17	18	4.3	LH	Dorsal Attention	Posterior 3
2	69	18	2.3	RH	Dorsal Attention	Posterior 4
3	18	17	4.1	LH	Dorsal Attention	Posterior 4
4	37	16	3.8	LH	Default Mode	Temporal 1
5	23	15	3.2	LH	Salience/Ventral Attention	Parietal Operculum 1
6	33	13	3.4	LH	Control	Parietal 1
7	73	9	2.8	RH	Salience/Ventral Attention	Temporal Occipital Parietal 1
8	36	8	3.1	LH	Control	Cingulate 1
9	28	8	1.8	LH	Salience/Ventral Attention	Medial 2
10	30	6	2.2	LH	Limbic	Orbital Frontal Cortex 1

Table 3. Top 10 Most Frequent Hub Regions (N Group Lower Dwell Time clusters). ROI indices and region names correspond to the Schaefer (2018) 100-parcel atlas. The *Freq* column shows frequency across seeds, and the *Avg Conn* column indicates average connectivity strength for that region.

Rank	ROI	Freq	Avg Conn	Hemi	Network	Atlas Region
1	69	10	3.3	RH	Dorsal Attention	Posterior 4
2	17	10	3.4	LH	Dorsal Attention	Posterior 3
3	23	10	3.5	LH	Salience/Ventral Attention	Parietal Operculum 1
4	73	9	2.0	RH	Salience/Ventral Attention	Temporal Occipital Parietal 1
5	75	8	2.0	RH	Salience/Ventral Attention	Frontal Operculum 1
6	44	8	2.0	LH	Default Mode	Prefrontal Cortex 4
7	30	8	2.8	LH	Limbic	Orbital Frontal Cortex 1
8	52	7	2.0	RH	Visual	Visual Cortex 3
9	94	5	3.0	RH	Default Mode	Ventral Prefrontal Cortex 2
10	31	5	3.4	LH	Limbic	Temporal Pole 1

and 4(b) provide visualizations of these hub locations. Notably, the Dorsal Attention, Salience/Ventral Attention, and Default Mode networks were predominantly represented among the top five regions in both cluster configurations: each of these networks contributes at least two regions to the top-five lists, and several of those regions exhibit high average connectivity (up to 4.3), supporting their role as core hubs within the identified clusters.

To evaluate whether hubness configuration differed between these two clusters, we performed a chi-squared test of independence on the hub frequency distributions. A total of 39 unique regions of interest (ROIs) were identified across the top 10 rankings in both conditions, resulting in 38 degrees of freedom for the test. The analysis revealed a significant overall difference in the distribution of hub frequencies between the two clusters ($\chi^2(38) = 94.03$, $p < 0.001$), indicating that the global pattern of brain regions acting as hubs was significantly associated with respect to the cluster type. To explore which regions contributed most to this effect, we conducted a post-hoc analysis of the standardized residuals for each ROI. A residual magnitude exceeding ± 1.96 was considered statistically significant ($p < 0.05$). No individual ROI surpassed this threshold, suggesting that no single region disproportionately influenced the overall χ^2 result. Instead, the observed group difference likely reflects a diffuse reorganization across multiple regions, where many small changes in hub presence collectively contribute to the significant global effect. Overall, these findings suggest that differences in dwell-time features reflect a subtle, distributed reorganization of hub dynamics.

Importantly, these statistical dwell-time findings show associative patterns rather than causal relationships. Although we cannot establish directionality between brain connectivity and genotype, the systematic differences in dwell-time features provide discriminative ability that can be exploited for genotype prediction and further interpretation. To test this, we used logistic regression, which provides both predictive performance and interpretability. The sign and magnitude of each coefficient, and the corresponding odds ratio, describe how the odds of a genotype change for a one-unit (16s) increase in a feature, providing a clear effect-size interpretation. In the subsequent machine-learning analysis, we therefore evaluate predictive performance and report coefficients and odds ratios to identify robustness and interpretability of dwell-time features.

K. Machine Learning

K.1. Classification Performance. We evaluated whether dwell-time features of dFC can predict APOE

Table 4. Model performance (mean ± std) for binary classification tasks. Results computed over subject-stratified 10-fold CV repeated 5 times.

Metric	N vs A+P-	N vs A+P+	A+P- vs A+P+	N vs (A+P- & A+P+)
Accuracy	0.608 ± 0.048	0.627 ± 0.037	0.507 ± 0.072	**0.647 ± 0.029**
Precision	0.615 ± 0.049	0.631 ± 0.041	0.509 ± 0.080	**0.631 ± 0.029**
Recall	0.614 ± 0.048	**0.635 ± 0.042**	0.509 ± 0.079	0.629 ± 0.025
F1 (macro)	0.607 ± 0.049	**0.623 ± 0.038**	0.503 ± 0.075	0.629 ± 0.026
AUC-ROC	0.606 ± 0.035	**0.631 ± 0.018**	0.531 ± 0.072	0.616 ± 0.018

Table 5. Logistic regression coefficient and odds-ratio statistics for clusters where the N group exhibited higher dwell-time than comparison groups. For the *A+P- vs. A+P+* task, the *A+P-* group showed higher dwell-time. Asterisks indicate FDR-adjusted p-values less than 0.05.

Task	**Count**	**Coef ± SE**	**OR ± SE**	**p (FDR)**
N vs. A+P-	122	-0.314 ± 0.111	0.731 ± 0.081	0.017*
N vs. A+P+	200	-0.267 ± 0.120	0.766 ± 0.092	0.047*
A+P- vs. A+P+	216	-0.299 ± 0.574	0.741 ± 0.426	0.603
N vs (A+P- & A+P+)	142	-0.262 ± 0.073	0.770 ± 0.057	0.004*

Table 6. Logistic regression coefficient and odds-ratio statistics for clusters where the A+P- groups or A+P+ exhibited higher dwell-time than the N group. For the *A+P- vs. A+P+* task, the *A+P+* group showed higher dwell-time. Asterisks indicate FDR-adjusted p-values less than 0.05.

Task	**Count**	**Coef ± SE**	**OR ± SE**	**p (FDR)**
N vs. A+P-	178	0.191 ± 0.090	1.211 ± 0.109	0.048*
N vs. A+P+	100	0.133 ± 0.060	1.142 ± 0.069	0.047*
A+P- vs. A+P+	84	0.060 ± 0.081	1.062 ± 0.085	0.524
N vs (A+P- & A+P+)	158	0.153 ± 0.056	1.166 ± 0.065	0.017*

ε4/PICALM genotype categories by training binary logistic regression models with subject-stratified 10-fold cross-validation repeated five times. Performance across the four classification tasks was modest yet reliably above chance, especially for comparisons including APOE-ε4 and PICALM rs3851179 non-carriers (N; Table 4). The strongest discrimination was observed for N vs. (A+P- & A+P+) with an accuracy of 0.647 ± 0.029, and for N vs. A+P+ which yielded the highest recall, macro-F1, and AUC-ROC (0.635 ± 0.042, 0.623 ± 0.038, and 0.631 ± 0.018, respectively). In contrast, in classification task, A+P- vs. A+P+ performance was chance-level (accuracy 0.507 ± 0.072; AUC-ROC 0.531 ± 0.072), indicating limited separability between single- and double-risk genotypes using dwell-time features alone.

K.2. Coefficient Orientation.. To interpret where a discriminative dwell-time arises, we summarized logistic regression coefficients and odds ratios (OR) over clusters that showed consistent dwell-time orientation. For instance, in *Direction 1* (clusters where N exhibited higher dwell-time than the comparison group; for *A+P- vs. A+P+*, clusters where A+P- exceeded A+P+), coefficients were negative with OR < 1 (Table 5). Across these clusters, several contrasts reached FDR significance: N vs. A+P- (Count = 122; Coef -0.314 ± 0.111, OR 0.731 ± 0.081, $p_{FDR} = 0.017^*$), N vs. A+P+ (Count = 200; Coef -0.267 ± 0.120, OR 0.766 ± 0.092, $p_{FDR} = 0.047^*$), and the combined contrast N vs. (A+P- & A+P+) (Count = 142; Coef -0.262 ± 0.073, OR 0.770 ± 0.057, $p_{FDR} = 0.004^*$). The A+P- vs. A+P+ contrast did not reach significance (Count = 216; $p_{FDR} = 0.603$). These negative coefficients indicate that increased dwell-time in clusters where the N group showed higher dwell-time was associated with lower odds of carrying the APOE-ε4 risk allele.

On the other hand, in *Direction 2* (clusters where A+P- or A+P+ exhibited higher dwell-time than N; for *A+P- vs. A+P+*, clusters where A+P+ exceeded A+P-), coefficients were positive with OR > 1 and several contrasts involving N showed robust significance (Table 6). Specifically, N vs. A+P- (Count = 178; Coef 0.191 ± 0.090, OR 1.211 ± 0.109, $p_{FDR} = 0.048^*$), N vs. A+P+ (Count = 100; Coef 0.133 ± 0.060, OR 1.142 ± 0.069, $p_{FDR} = 0.047^*$), and the pooled contrast N vs. (A+P- & A+P+) (Count = 158; Coef 0.153 ± 0.056, OR 1.166 ± 0.065, $p_{FDR} = 0.017^*$) all reached FDR significance; the A+P- vs. A+P+ contrast did not (Count = 84; $p_{FDR} = 0.524$). Conversely, positive coefficients indicate that increased dwell-time in clusters where the A+P+ and A+P- groups showed higher dwell-time was associated with higher odds of carrying the APOE-ε4 risk allele.

K.3. Interpreting Odds Ratios. All coefficients and odds ratios were reported per 16-second increase in dwell time. *Direction 1* clusters (N groups show higher dwell-time) OR < 1 indicated that greater dwell-time predicts membership in the N group vs Others. For example, N vs. A+P- (OR = 0.731) implies $\approx 37\%$ higher odds of being N per additional 16s; N vs. A+P+ (OR = 0.766) $\approx 31\%$ higher; combined N vs. (A+P- & A+P+) (OR = 0.770) $\approx 30\%$ higher (Table 5). On the other hand, *Direction 2* clusters (A+P+ show higher dwell-time) OR > 1 indicated greater dwell-time predicts the risk group (i.e., lower odds of being N). For example, N vs. A+P-

Table 7. Summary of Classification Performance and Permutation Test Results.

Comparison	Observed AUC ↑	Empirical p-value ↓
N vs. A+P-	0.608	0.118
N vs. A+P+	**0.631**	0.102
A+P- vs. A+P+	0.531	0.335
N vs. (A+P- & A+P+)	0.616	**0.078**

(OR = 1.211) implies $\approx 17\%$ lower odds of being N per 16 s; N vs. A+P+ (OR = 1.142) $\approx 12\%$ lower; combined N vs. (A+P- & A+P+) (OR = 1.166) $\approx 14\%$ lower (Table 6).

The effects were robust and recurrent across folds and k values: Direction 1 clusters occurred 122, 200, and 142 times for N vs. A+P-, N vs. A+P+, and pooled N vs. risk-groups, respectively, and these N group contrasts reached FDR significance. Direction 2 clusters (178, 100, 158) also produced significant N-related contrasts. By contrast, A+P- vs. A+P+ did not reach significance in either direction ($p_{\mathrm{FDR}} = 0.603$ and 0.524), suggesting that APOE-$\varepsilon 4$ status (A+ vs. A-) drives the primary differences from N. In contrast, PICALM rs3851179 (P+) status alone does not reliably differentiate the risky groups.

K.4. Permutation Test. To assess whether dFC dwell-time features could reliably classify subject groups, we implemented a separate machine learning pipeline and evaluated its statistical significance using a rigorous, non-parametric permutation testing framework with 1000 permutations. The classification performance, measured by the AUC, and corresponding empirical p-values for each comparison are summarized in Table 7. Our analysis revealed that while classification performance was consistently above chance for most of the tasks, none of the comparisons reached the conventional threshold for statistical significance ($p < 0.05$). The highest classification performance was observed for the N vs. A+P+ comparison (AUC = 0.631). But, the permutation test (genotype label shuffling) demonstrated that this result was not statistically significant ($p = 0.102$), indicating a trend that did not meet our pre-defined significance level. A similar finding was observed between N vs. A+P- subjects (AUC = 0.608, $p = 0.118$) and between A+P- vs. A+P+ (AUC = 0.531, $p = 0.335$), which was also not statistically significant. Interestingly, when the risk groups are combined against the N group (N vs. A+P- and A+P+), a trend toward significance was seen at AUC = 0.616 and $p = 0.078$, indicating that the larger sample size could potentially enable the permutation test to reach significance, especially for comparison between N vs A+P- and N vs A+P+.

Discussion

Our analysis of dFC clusters revealed a consistent bidirectional pattern that showed robustness across different numbers of clusters (k = 5—10) and multiple random seeds. Rather than identifying two specific, distinct clusters, we observed that cluster formations consistently segregated into two opposing directions: clusters where the not-at-risk (N) group exhibited higher dwell time relative to at-risk groups (A+P- and A+P+), and clusters where at-risk groups showed higher dwell time than N. We evaluated whether a given cluster orientation (N $>$ A+P- and/or A+P+ versus N $<$ A+P- and/or A+P+) recurred systematically across different clusters, rather than relying on specific cluster labels from any single (k) value. This approach revealed that both directions were consistently represented across k values. Most clusters showed clear separation of their corresponding centroids (see Figure 3), supporting their interpretation as functionally distinct brain clusters rather than clustering artifacts. It is important to note that we did not select specific k values and clusters for our analysis. Instead, we chose them empirically and independently of any statistical findings based on the resulting clustering. This shows that our results are not biased towards any particular configuration and are reliable and reproducible (code available on GitHub).

For the interpretation of these clusters, which showed recurring directional patterns, we identified the most influential brain regions (hubs) across all clusters contributing to each direction. Notably, the top-10 hubs with the largest proportional contributions were predominantly left-lateralized, specifically in clusters where the N group exhibited higher dwell-time.

This pronounced left-hemisphere lateralization of key dFC clusters aligns remarkably with a large body of literature on the asymmetrical nature of AD pathology. Although our findings do not imply a direct causal link between dwell times and AD pathophysiology, they provide compelling correlational evidence. It is well-documented that brain atrophy in AD often develops unevenly, disrupting normal brain asymmetry (Friedland et al., 1988). Multiple studies have reported that cortical thinning, Aβ deposits, and neurite connectivity loss are more pronounced in the left hemisphere of AD patients (Lubben et al., 2021; Roe et al., 2021). This structural degradation is often accompanied by functional changes; for instance, a shift toward rightward asymmetry in white-matter networks has been interpreted as a consequence of left-hemisphere impairment in AD (Yang et al., 2017). Similarly, functional near-infrared spectroscopy (fNIRS) studies, which also measure hemodynamic responses, have observed reduced functional connectivity in AD patients, predominantly affecting left-hemisphere regions (Mızrak et al., 2024).

Our results contribute to this literature by demonstrating that dFC patterns may also reflect this left-hemisphere vulnerability in individuals at risk (in our study, this is an association with genetic factors) for AD. The identification of two directionally opposed, left-lateralized clusters could indicate a compensatory neural response emerging during the latent phase of AD progression,

which may temporarily protect against neurodegenerative changes, potentially modulated by amyloid-related mutations (Bobkova and Vorobyov, 2015). Having established this group-level neurobiological association, we next sought to determine if these dFC-derived dwell-time features contained sufficient information for individual-level genotype classification. Our initial ML models confirmed this potential, yielding modest but consistently above-chance classification performance (Table 4). The analysis was also highly interpretable; regression coefficients for specific brain clusters were significant after FDR correction. For direction 1 clusters, an increase in dwell time was associated with higher odds of being in the N group (e.g., a nearly 37% increase in odds per 16s), while for others, the inverse was true (Table 5 & 6). However, given that the overall classification performance was modest, it was critical to assess whether this predictive accuracy was statistically robust or simply a product of chance. We formally tested this using a comprehensive permutation framework (1000 permutations), where the observed model AUC was compared against a null distribution generated from models trained on randomly permuted genotype labels.

The permutation test revealed a trend toward significance for the combined contrast N vs. (A+P- & A+P+) ($p = 0.078$) using the full sample size of the dataset. Although this result does not meet the conventional $p < 0.05$ threshold, it indicates a marginal effect: dwell-time features capture subtle genotype-related variation. Combined with the non-significant A+P- vs. A+P+ contrasts, these findings suggest that APOE-$\varepsilon 4$ (A+), rather than PICALM rs3851179 (P+) status, may drive the primary differences from the N group. While this does not constitute a validated biomarker, it supports further work with larger cohorts.

Finally, it is important to note the limitations of our study. First, the sample size is modest, totalling 68 subjects, which may limit statistical power. Also, the use of 10–fold cross-validation may have hindered some statistical advantage over the utilization of leave-one-subject-out cross-validation for significant cluster selection for the permutation tests. Second, the current method relies only on rs-fMRI data. Structural MRI features, such as volumetric mapping and cortical thickness, could further enhance our analysis by capturing anatomical variations underlying functional changes. Furthermore, EEG, with its high temporal resolution, could provide a complementary perspective. A future multimodal framework could therefore improve performance, though likely at the cost of increased interpretational complexity. Finally, we re-emphasize that this is an association study. We have observed a correlation between a dFC-derived feature and genetic risk groups, and future work should remain cautious about inferring any direct causal links.

These findings represent a step forward in understanding dFC patterns and their features associated with the genetic risk of AD. The convergent neuroanatomical evidence, particularly the consistent left-hemispheric hub patterns, provides valuable insights for future studies. Our promising results, therefore, can motivate future studies on larger cohorts and multimodal extensions that can further enhance our understanding of preclinical or early AD pathophysiology.

Conclusion

Our study used dFC with k-means clustering to extract dwell-time features. The dwell-time features in two recurring clusters enabled discrimination between individuals who are not at risk (N) and those at-risk of higher genetic risk (carriers of APOE-$\varepsilon 4$ or PICALM rs3851179 risk alleles) for AD. These two directionally opposite dFC clusters, one in which N $>$ (A+P- and A+P+) and the other in which N $<$ (A+P- and A+P+) were consistent across $k = 5 - 10$. Hubness analysis showed a left-hemisphere bias in the top ten hubs, aligning with prior studies of asymmetric AD vulnerability. Although classification based on dwell-time produced only modest performance, permutation testing revealed a trend suggesting that a larger sample size may achieve statistically significant prediction. Overall, these results provide correlational evidence linking dwell-time patterns to APOE-$\varepsilon 4$/PICALM genotype and highlight the importance of performing follow-up longitudinal studies.

Bibliography

Agosta, F., Pievani, M., Geroldi, C., Copetti, M., Frisoni, G. B., and Filippi, M. (2012). Resting state fmri in alzheimer's disease: beyond the default mode network. *Neurobiology of Aging*, 33(8):1564–1578. doi: https://doi.org/10.1016/j.neurobiolaging.2011.06.007.

Allen, E. A., Damaraju, E., Plis, S. M., Erhardt, E. B., Eichele, T., and Calhoun, V. D. (2012). Tracking whole-brain connectivity dynamics in the resting state. *Cerebral Cortex*, 24(3): 663–676. doi: 10.1093/cercor/bhs352.

Allen, G., Barnard, H., McColl, R., Hester, A. L., Fields, J. A., Weiner, M. F., Ringe, W. K., Lipton, A. M., Brooker, M., McDonald, E., Rubin, C. D., and Cullum, C. M. (2007). Reduced hippocampal functional connectivity in alzheimer disease. *Archives of Neurology*, 64(10):1482–1487. doi: 10.1001/archneur.64.10.1482.

Andersson, J. L., Skare, S., and Ashburner, J. (2003). How to correct susceptibility distortions in spin-echo echo-planar images: application to diffusion tensor imaging. *NeuroImage*, 20(2):870–888. doi: https://doi.org/10.1016/S1053-8119(03)00336-7.

Andrews-Hanna, J. R., Reidler, J. S., Sepulcre, J., Poulin, R., and Buckner, R. L. (2010). Functional-anatomic fractionation of the brain's default network. *Neuron*, 65(4):550–562. doi: 10.1016/j.neuron.2010.02.005.

Bobkova, N. and Vorobyov, V. (2015). The brain compensatory mechanisms and alzheimer's disease progression: a new protective strategy. *Neural regeneration research*, 10(5): 696–697. doi: 10.4103/1673-5374.156954.

Breijyeh, Z. and Karaman, R. (2020). Comprehensive review on alzheimer's disease: Causes and treatment. *Molecules*, 25(24). doi: 10.3390/molecules25245789.

Brion, J.-P. (1998). Neurofibrillary tangles and alzheimer's disease. *European neurology*, 40 (3):130–140. doi: 10.1159/000007969.

Dzianok, P. and Kublik, E. (2024). Pearl-neuro database: Eeg, fmri, health and lifestyle data of middle-aged people at risk of dementia. *Scientific Data*, 11(1):276. doi: 10.1038/s41597-024-03106-5.

Dzianok, P., Wojciechowski, J., Wolak, T., and Kublik, E. (2025). Alzheimer's disease-like features in resting state eeg/fmri of cognitively intact and healthy middle-aged apoe/picalm risk carriers. *Journal of Alzheimer's Disease*, 104(2):509–524. doi: 10.1177/13872877251317489. PMID: 40095677.

Dzianok, P., Wojciechowski, J., Wolak, T., and Kublik, E. (2025). Alzheimer's disease-like features in resting state eeg/fmri of cognitively intact and healthy middle-aged apoe/picalm risk carriers. *Journal of Alzheimer's Disease*, 104(2):509–524. doi: 10.1177/13872877251317489. PMID: 40095677.

Esteban, O., Markiewicz, C. J., Blair, R. W., Moodie, C. A., Isik, A. I., Erramuzpe, A., Kent, J. D., Goncalves, M., DuPre, E., Snyder, M., et al. (2019). fmriprep: a robust preprocessing pipeline for functional mri. *Nature methods*, 16(1):111–116. doi: 10.1038/s41592-018-0235-4.

Esteban, O., Ciric, R., Finc, K., Blair, R. W., Markiewicz, C. J., Moodie, C. A., Kent, J. D., Goncalves, M., DuPre, E., Gomez, D. E., et al. (2020). Analysis of task-based functional

mri data preprocessed with fmriprep. *Nature protocols*, 15(7):2186–2202. doi: 10.1038/s41596-020-0327-3.

Fonov, V., Evans, A., McKinstry, R., Almli, C., and Collins, D. (2009). Unbiased nonlinear average age-appropriate brain templates from birth to adulthood. *NeuroImage*, 47:S102. doi: https://doi.org/10.1016/S1053-8119(09)70884-5. Organization for Human Brain Mapping 2009 Annual Meeting.

Fonov, V., Evans, A. C., Botteron, K., Almli, C. R., McKinstry, R. C., Collins, D. L., Group, B. D. C., et al. (2011). Unbiased average age-appropriate atlases for pediatric studies. *Neuroimage*, 54(1):313–327. doi: 10.1016/j.neuroimage.2010.07.033.

Friedland, R. P., Koss, E., Haxby, J. V., Grady, C. L., Luxenberg, J., Schapiro, M. B., and Kaye, J. (1988). Alzheimer disease: Clinical and biological heterogeneity. *Annals of internal medicine*, 109(4):298–311. doi: 10.7326/0003-4819-109-4-298.

Gong, C., Song, W., Zhu, Z., Yang, D., Zhao, X., Xu, Y., and Zhao, H. (2025). Apoe ε4 influences the dynamic functional connectivity variability and cognitive performance in alzheimer's disease. *Journal of Alzheimer's Disease*, 104(4):1103–1114. doi: https://doi.org/10.1177/13872877251322687.

Greicius, M. D., Srivastava, G., Reiss, A. L., and Menon, V. (2004). Default-mode network activity distinguishes alzheimer's disease from healthy aging: evidence from functional mri. *Proceedings of the National Academy of Sciences*, 101(13):4637–4642. doi: 10.1073/pnas.0308627101.

Hutchison, R. M., Womelsdorf, T., Allen, E. A., Bandettini, P. A., Calhoun, V. D., Corbetta, M., Della Penna, S., Duyn, J. H., Glover, G. H., Gonzalez-Castillo, J., Handwerker, D. A., Keilholz, S., Kiviniemi, V., Leopold, D. A., de Pasquale, F., Sporns, O., Walter, M., and Chang, C. (2013). Dynamic functional connectivity: Promise, issues, and interpretations. *NeuroImage*, 80:360–378. doi: https://doi.org/10.1016/j.neuroimage.2013.05.079. Mapping the Connectome.

Jack, C. R., Knopman, D. S., Jagust, W. J., Petersen, R. C., Weiner, M. W., Aisen, P. S., Shaw, L. M., Vemuri, P., Wiste, H. J., Weigand, S. D., Lesnick, T. G., Pankratz, V. S., Donohue, M. C., and Trojanowski, J. Q. (2013). Tracking pathophysiological processes in alzheimer's disease: an updated hypothetical model of dynamic biomarkers. *The Lancet Neurology*, 12(2):207–216. doi: https://doi.org/10.1016/S1474-4422(12)70291-0.

Jack, J., Clifford R., Therneau, T. M., Weigand, S. D., Wiste, H. J., Knopman, D. S., Vemuri, P., Lowe, V. J., Mielke, M. M., Roberts, R. O., Machulda, M. M., Graff-Radford, J., Jones, D. T., Schwarz, C. G., Gunter, J. L., Senjem, M. L., Rocca, W. A., and Petersen, R. C. (2019). Prevalence of biologically vs clinically defined alzheimer spectrum entities using the national institute on aging–alzheimer's association research framework. *JAMA Neurology*, 76(10):1174–1183. doi: 10.1001/jamaneurol.2019.1971.

Jezzard, P. and Balaban, R. S. (1995). Correction for geometric distortion in echo planar images from b0 field variations. *Magnetic resonance in medicine*, 34(1):65–73. doi: 10.1002/mrm.1910340111.

Jones, D. T., Vemuri, P., Murphy, M. C., Gunter, J. L., Senjem, M. L., Machulda, M. M., Przybelski, S. A., Gregg, B. E., Kantarci, K., Knopman, D. S., Boeve, B. F., Petersen, R. C., and Jack, C. R., Jr. (2012). Non-stationarity in the "resting brain's" modular architecture. *PLOS ONE*, 7(6):1–15. doi: 10.1371/journal.pone.0039731.

Langbaum, J. B., Ellison, N. N., Caputo, A., Thomas, R. G., Langlois, C., Riviere, M.-E., Graf, A., Lopez Lopez, C., Reiman, E. M., Tariot, P. N., et al. (2020). The alzheimer's prevention initiative composite cognitive test: a practical measure for tracking cognitive decline in preclinical alzheimer's disease. *Alzheimer's research & therapy*, 12:1–11. doi: 10.1186/s13195-020-00633-2.

Lee, P.-L., Chou, K.-H., Chung, C.-P., Lai, T.-H., Zhou, J. H., Wang, P.-N., and Lin, C.-P. (2020). Posterior cingulate cortex network predicts alzheimer's disease progression. *Frontiers in aging neuroscience*, 12:608667. doi: 10.3389/fnagi.2020.608667.

Li, S.-J., Li, Z., Wu, G., Zhang, M.-J., Franczak, M., and Antuono, P. G. (2002). Alzheimer disease: evaluation of a functional mr imaging index as a marker. *Radiology*, 225(1): 253–259. doi: https://doi.org/10.1148/radiol.2251011301.

Lubben, N., Ensink, E., Coetzee, G. A., and Labrie, V. (2021). The enigma and implications of brain hemispheric asymmetry in neurodegenerative diseases. *Brain communications*, 3(3):fcab211. doi: 10.1093/braincomms/fcab211.

M Di Battista, A., M Heinsinger, N., and William Rebeck, G. (2016). Alzheimer's disease genetic risk factor apoe-ε4 also affects normal brain function. *Current Alzheimer Research*, 13(11):1200–1207. doi: 10.2174/1567205013666160401115127.

Mızrak, H. G., Dikmen, M., Hanoğlu, L., and Şakul, B. U. (2024). Investigation of hemispheric asymmetry in alzheimer's disease patients during resting state revealed by fnirs. *Scientific Reports*, 14(1):13454. doi: 10.1038/s41598-024-62281-y.

Morgen, K., Ramirez, A., Frölich, L., Tost, H., Plichta, M. M., Kölsch, H., Rakebrandt, F., Rienhoff, O., Jessen, F., Peters, O., et al. (2014). Genetic interaction of picalm and apoe is associated with brain atrophy and cognitive impairment in alzheimer's disease. *Alzheimer's & Dementia*, 10:S269–S276. doi: https://doi.org/10.1016/j.jalz.2013.11.001.

O'Callaghan, C., Shine, J. M., Hodges, J. R., Andrews-Hanna, J. R., and Irish, M. (2019). Hippocampal atrophy and intrinsic brain network dysfunction relate to alterations in mind wandering in neurodegeneration. *Proceedings of the National Academy of Sciences*, 116 (8):3316–3321. doi: 10.1073/pnas.1818523116.

Palmqvist, S., Schöll, M., Strandberg, O., Mattsson, N., Stomrud, E., Zetterberg, H., Blennow, K., Landau, S., Jagust, W., and Hansson, O. (2017). Earliest accumulation of β-amyloid occurs within the default-mode network and concurrently affects brain connectivity. *Nature communications*, 8(1):1214. doi: 10.1038/s41467-017-01150-x.

Ponomareva, N., Andreeva, T., Protasova, M., Konovalov, R., Krotenkova, M., Malina, D., Mitrofanov, A., Fokin, V., Illarioshkin, S., and Rogaev, E. (2020). Genetic association between alzheimer's disease risk variant of the picalm gene and eeg functional connectivity in non-demented adults. *Frontiers in neuroscience*, 14:324. doi: https://doi.org/10.3389/fnins.2020.00324.

Preti, M. G., Bolton, T. A., and Van De Ville, D. (2017). The dynamic functional connectome: State-of-the-art and perspectives. *NeuroImage*, 160:41–54. doi: https://doi.org/10.1016/j.neuroimage.2016.12.061. Functional Architecture of the Brain.

Raichle, M. E. (2015). The brain's default mode network. *Annual review of neuroscience*, 38(1):433–447. doi: https://doi.org/10.1146/annurev-neuro-071013-014030.

Raichle, M. E., MacLeod, A. M., Snyder, A. Z., Powers, W. J., Gusnard, D. A., and Shulman, G. L. (2001). A default mode of brain function. *Proceedings of the National Academy of Sciences*, 98(2):676–682. doi: 10.1073/pnas.98.2.676.

Rao, Y. L., Ganaraja, B., Murlimanju, B., Joy, T., Krishnamurthy, A., and Agrawal, A. (2022). Hippocampus and its involvement in alzheimer's disease: a review. *3 Biotech*, 12(2):55. doi: 10.1007/s13205-022-03123-4.

Roe, J. M., Vidal-Piñeiro, D., Sørensen, Ø., Brandmaier, A. M., Düzel, S., Gonzalez, H. A., Kievit, R. A., Knights, E., Kühn, S., Lindenberger, U., et al. (2021). Asymmetric thinning of the cerebral cortex across the adult lifespan is accelerated in alzheimer's disease. *Nature communications*, 12(1):721. doi: 10.1038/s41467-021-21057-y.

Scharre, D. W. (2019). Preclinical, prodromal, and dementia stages of alzheimer's disease. *Pract Neurol*, 15:36–47.

Sheline, Y. I., Morris, J. C., Snyder, A. Z., Price, J. L., Yan, Z., D'Angelo, G., Liu, C., Dixit, S., Benzinger, T., Fagan, A., et al. (2010). Apoe4 allele disrupts resting state fmri connectivity in the absence of amyloid plaques or decreased csf aβ42. *Journal of neuroscience*, 30 (50):17035–17040. doi: 10.1523/JNEUROSCI.3987-10.2010.

Small, S. A., Schobel, S. A., Buxton, R. B., Witter, M. P., and Barnes, C. A. (2011). A pathophysiological framework of hippocampal dysfunction in ageing and disease. *Nature Reviews Neuroscience*, 12(10):585–601. doi: 10.1038/nrn3085.

Wang, X., Wang, J., He, Y., Li, H., Yuan, H., Evans, A., Yu, X., He, Y., and Wang, H. (2015). Apolipoprotein e ε4 modulates cognitive profiles, hippocampal volume, and resting-state functional connectivity in alzheimer's disease. *Journal of Alzheimer's Disease*, 45(3): 781–795. doi: 10.3233/JAD-142556. PMID: 25624419.

Xu, W., Tan, L., and Yu, J.-T. (2015). The role of picalm in alzheimer's disease. *Molecular neurobiology*, 52(1):399–413. doi: https://doi.org/10.1007/s12035-014-8878-3.

Yang, C., Zhong, S., Zhou, X., Wei, L., Wang, L., and Nie, S. (2017). The abnormality of topological asymmetry between hemispheric brain white matter networks in alzheimer's disease and mild cognitive impairment. *Frontiers in aging neuroscience*, 9:261. doi: 10.3389/fnagi.2017.00261.

Zhang, P., Qin, W., Wang, D., Liu, B., Zhang, Y., Jiang, T., and Yu, C. (2015). Impacts of picalm and clu variants associated with alzheimer's disease on the functional connectivity of the hippocampus in healthy young adults. *Brain Structure and Function*, 220:1463–1475. doi: 10.1007/s00429-014-0738-4.

Zhao, C., Huang, W.-J., Feng, F., Zhou, B., Yao, H.-X., Guo, Y.-E., Wang, P., Wang, L.-N., Shu, N., and Zhang, X. (2022). Abnormal characterization of dynamic functional connectivity in alzheimer's disease. *Neural regeneration research*, 17(9):2014–2021. doi: https://doi.org/10.4103/1673-5374.332161.

Zhou, J., Greicius, M. D., Gennatas, E. D., Growdon, M. E., Jang, J. Y., Rabinovici, G. D., Kramer, J. H., Weiner, M., Miller, B. L., and Seeley, W. W. (2010). Divergent network connectivity changes in behavioural variant frontotemporal dementia and alzheimer's disease. *Brain*, 133(5):1352–1367. doi: 10.1093/brain/awq075.

Zhou, Y., Dougherty Jr, J. H., Hubner, K. F., Bai, B., Cannon, R. L., and Hutson, R. K. (2008). Abnormal connectivity in the posterior cingulate and hippocampus in early alzheimer's disease and mild cognitive impairment. *Alzheimer's & Dementia*, 4(4):265–270. doi: 10.1016/j.jalz.2008.04.006.